



Deep-learning-based isogeometric inverse design for tetra-chiral auxetics

Zhongyuan Liao^a, Yingjun Wang^{a,b,*}, Liang Gao^b, Zhen-Pei Wang^{c,**}

^a National Engineering Research Center of Novel Equipment for Polymer Processing, The Key Laboratory of Polymer Processing Engineering of the Ministry of Education, Guangdong Provincial Key Laboratory of Technique and Equipment for Macromolecular Advanced Manufacturing, South China University of Technology, Guangzhou, 510641, China

^b State Key Laboratory of Digital Manufacturing Equipment and Technology, Huazhong University of Science and Technology, Wuhan, 430074, China

^c Institute of High Performance Computing (IHPC), Agency for Science, Technology and Research (A*STAR), 1 Fusionopolis Way, 138632, Singapore

ARTICLE INFO

Keywords:

Deep neural networks
Negative Poisson's ratio
Chiral auxetics
Inverse design
Shape optimization
Isogeometric analysis

ABSTRACT

Auxetic materials with the counter-intuitive effect of negative Poisson's ratio (NPR) have potentials for diverse applications. Typical shape optimization designs of auxetic structures involve complicated sensitivity analysis and a time-consuming iterative process, which is not beneficial for designing functionally-graded structures where the auxetics at different locations need to be inversely designed. To improve the efficiency of the inverse design and simplify the sensitivity analysis, we propose a deep-learning-based inverse shape design approach for tetra-chiral auxetics. First, a non-uniform rational basis spline (NURBS)-based parameterization of tetra-chiral structures is developed to create design samples and computational homogenization based on isogeometric analysis is used in these samples to generate a database consisting of mechanical properties and geometric parameters. Then, the database is utilized to train deep neural networks (DNN) to generate a surrogate model that represents the effective mechanical properties as a function of geometric parameters. Finally, the surrogate model is directly used in the inverse design framework where sensitivity analysis can be calculated analytically. Numerical examples with verifications are presented to demonstrate the efficiency and accuracy of the proposed design methodology.

1. Introduction

The positive Poisson's ratio is the physical properties for most materials in nature, following the rule that expanding when compressed and shrinking when stretched. These materials are normally referred to as conventional materials with Poisson's ratio value ranging from 0 to 0.5 [1–3]. Based on classical elasticity theory, the available values of Poisson's ratio are from -1 to 0.5 for 3D isotropic materials and from -1 to 1 for 2D isotropic systems with thermodynamic consideration of strain energy [4]. Some special natural materials expand in the orthogonal direction when stretched and shrink when compressed, exhibiting a negative Poisson's ratio (NPR), such as crystalline materials [5,6], rock with micro-cracks [7], cancellous bone [8] and cat skin [9,10]. This auxeticity behavior can also be achieved by engineering the architected materials with auxetic units [11–14]. In 1985, Almgren [12] designed a rod-hinge-spring structure to achieve auxetic behavior ($\nu = -1$). In the same year, Kolpakov [11] presented a lattice structure with re-entrant honeycomb features to obtain auxetic performances. The

polymer foams with negative Poisson's ratio were discovered later by Lakes [15]. These pioneering works drew wide attention in academic field to study the auxetics. The term auxetic in the scientific literature was introduced by Evans [16] in 1991. One of the commonly-studied architected auxetics is the chiral auxetics, which has the significant characteristic that does not superimpose with their mirror images. The first isotropic 2D chiral molecular models (spontaneously forming auxetic phases) were studied by Wojciechowski using computational simulations [17] and analytic methods [18]. Then, Lakes et al. [19] proposed a hexagonal honeycomb pattern consisting of central circles with tangentially attached ligaments to achieve the chirality. A tetra-chiral auxetic system can even achieve auxetic, partially auxetic, and nonauxetic behavior on the molecular level [20]. More research about chiral-auxetic structures can be found in [21–23]. The auxeticity achieved in chiral configuration is mainly based on the deformation of rotating ligaments. In addition, the chiral structures allow unit cells more easily to interlock under the condition of periodic boundary [24],

* Corresponding author at: National Engineering Research Center of Novel Equipment for Polymer Processing, The Key Laboratory of Polymer Processing Engineering of the Ministry of Education, Guangdong Provincial Key Laboratory of Technique and Equipment for Macromolecular Advanced Manufacturing, South China University of Technology, Guangzhou, 510641, China.

** Corresponding author at: Institute of High Performance Computing (IHPC), Agency for Science, Technology and Research (A*STAR), 1 Fusionopolis Way, 138632, Singapore.

E-mail addresses: wangyj84@scut.edu.cn (Y. Wang), wangzp@ihpc.a-star.edu.sg (Z.-P. Wang).

<https://doi.org/10.1016/j.compstruct.2021.114808>

Received 20 June 2021; Received in revised form 6 October 2021; Accepted 9 October 2021

Available online 27 October 2021

0263-8223/© 2021 Elsevier Ltd. All rights reserved.

have the resistance to disorder [25] and more robust performance of auxeticity under manufacturing errors with both small and large deformation [26].

Due to their auxeticity, auxetic structures exhibit various beneficial phenomena, such as increasing indentation resistance and plane strain fracture toughness, the enhancement of shear stiffness, and improvement on the energy absorption properties [27,28], with applications found in sports and textiles [29,30], aerospace industry [31] and sensors or actuators [32].

Designing auxetic structures using numerical simulations has two broad approaches. One is to design the structures based on an in-depth understanding of the deformation mechanisms of certain types of structures, such as structures with features of star-shaped [33,34], re-entrant [35,36], chiral [19,37], star-shaped pores [38], rotating polygons/polyhedrons [39,40] and those with buckling mechanisms [41–43]. The details can be referred to recent works [13,14,44]. This category needs to set a referenced configuration, through changing some essential features of components to control the auxeticity. However, the initial configurations generally rely on substantial prior knowledge of experienced designers, limiting broad applications of auxetic materials. The other is numerical optimization techniques, mainly based on topology optimization [24,45–49], shape and size optimization [50–53].

To achieve an integrated design, analysis and manufacturing system, the isogeometric analysis (IGA) demonstrates a great flexibility and potential in structure design optimization [54], which has triggered renewed interests in designing auxetic lattices using shape and size optimization [52,53,55,56].

Despite of the extraordinary advantages of designing the auxetic lattices using isogeometric analysis, the challenge of performing highly efficient sensitivity analyses remains to be an inevitable obstacle for fast inverse design problems [53], which is not favored in designing functionally-graded structures involving multi-scale inverse search algorithms [57–59].

To improve the efficiency of the inverse design process of chiral auxetics with target material properties, we utilize machine learning approach to predict the properties of material and structures, such that the time cost in the computational homogenization and the sensitivity analysis can be significantly reduced. Predicting material properties using machine learning has been widely used in literature, such as neural networks for hyperelastic materials [60], convolutional neural networks for composite [61], deep material networks for 2D and 3D heterogeneous materials [62,63], clustering discretization methods for heterogeneous materials [64] and generative adversarial networks for architected materials [65]. Recently, Wilt et al. [66] used deep learning method to accelerate the auxetic design process, which can bypass potentially complex hyperelastic analytical methods. Kollmann et al. [67] proposed a deep-learning-based optimization for bulk modulus, shear modulus, or Poisson's ratio. Wang et al. [68] designed a novel planar perforated auxetic metamaterial with orthogonally aligned oval holes, which can be analyzed by machine learning method effectively.

Applying machine learning to topology optimization problems has also demonstrated certain potential, such as 3D topology optimization [69], speeding up methods for topology optimization [70], near-optimal topology optimization [71,72], moving morphable component-based structure optimization [73], optimization under variable loading configurations [74] and generative design [75]. As for shape optimization, Wang et al. [76] presented a back-propagation neural network to design auxetics. Compared with topology optimization, the number of design variables in shape optimization is tiny, advantaging in fewer training costs when combined with machine learning methods.

In this work, we seek to utilize deep learning (DL) techniques to solve the integrated shape and size optimization design problems for tetra-chiral auxetic structures, which has the following advantages:

- Effective computing. In most conventional designs, the mechanical properties analysis mainly used homogenization method accounting for huge computational resources. The DL can be utilized to learn the homogenization calculation in numerical simulation and fit a surrogate model to replace the homogenization calculation, reducing computing time significantly, which is of great interests for multi-scale inverse design problems that may require different local designs at different locations [57,58,77, 78].
- Concise sensitivity analysis. The relationship between geometric parameters and effective mechanical properties can be expressed in an explicit function, which brings a fast, straightforward, and analytical sensitivity analysis, which further speeds up the inverse design efficiency.

Here, we propose a deep-learning-based isogeometric inverse design for tetra-chiral auxetics. The framework of IGA enables a remarkable advantage of geometry modeling such that using only a small number of design variables can describe the complex chiral structures in a simple way. By introducing deep neural networks (DNN) to analyze massive simulation data of randomly generated configurations, the highly non-linear relationship between geometric parameters and effective mechanical properties can be expressed by an explicit analytical surrogate function, replacing the time-consuming homogenization calculation. Subjected to an effective stiffness constraint, an inverse design framework to achieve programmable auxetic designs with target properties is developed, and the design limit under different stiffness constraints is studied. Due to the IGA, the proposed method also achieves an integration between design, analysis, and manufacture.

The paper is organized as follows: the framework of the isogeometric inverse design is elaborated in Section 2. The training process of deep neural network is presented in Section 3. The results of numerical inverse design and verification studies are discussed in Section 4. Finally, some concluding remarks are provided in Section 5.

2. The framework of deep-learning-based isogeometric inverse design

2.1. Isogeometric encoding scheme

The pattern of a tetra-chiral structure proposed in this work has a core surrounded by four ligaments, the auxeticity and chirality are shown in Fig. 1a,b. The core is parameterized with 5×5 control points as a square, shown in Fig. 1c. A series of width parameters, w_i , with $i = 1, 2, 3, 4, 5$, and the offsetting parameters, o_i , with $i = 1, 2, 3$, are used to characterize the ligaments, as shown in Fig. 1c. It is noted that the width parameters represent the distance between the two boundary control points at different vertical locations; the offsetting parameters represent the offsetting value of the central control points from the centerline at different vertical locations; and $w_1 = 2d$. To ensure the periodicity, the top boundary center of ligaments should be fixed on the vertical centerline for tetra-chiral structures. The order of the NURBS utilized here is 3 (corresponding to the degree of 2), the knot vectors used for all design parameterizations are the same, $[0, 0, 0, 1/3, 2/3, 1, 1, 1]$. The additional parameter h in Fig. 1c denotes the ligament height and H equals to half of the unit side length. To obtain a full unit of a tetra-chiral structure, the four edges of the square core are aligned with four ligaments patterned in a circular fashion. The red part in Fig. 1c represents the minimum representative volume element (RVE) size of chiral structures. Given an RVE, imposing a macro strain with periodic boundary conditions on the structure, the effective mechanical properties can be calculated by using homogenization method detailed in Section 2.2.

With above NURBS parameterization scheme, the tetra-chiral structures can be encoded by 8 design parameters, i.e., $\chi = [w_1, w_2, w_3, w_4, w_5, o_1, o_2, o_3]$ including the size and shape parameters, leading to an

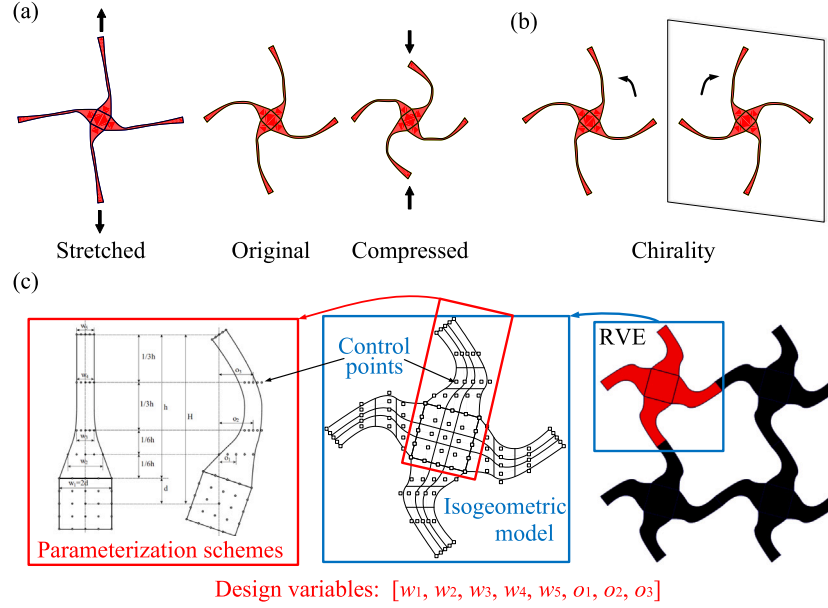


Fig. 1. Illustrations of the tetra-chiral auxetics: (a) the auxetic property, (b) the chirality, and (c) isogeometric encoding schemes.

integrated shape and size design optimization. Some samples with different encoding parameters are plotted in Fig. 2, which shows the excellent flexibility and broad design freedom of the proposed isogeometric encoding scheme. For simplicity, each RVE utilizes a dimension of 20×20 with a Young's modulus of 1 and a Poisson's ratio of 0.3, noting that the effective properties (e.g., the effective Young's modulus and Poisson's ratio) are non-dimensional.

2.2. IGA-based homogenization method

Given an RVE defined in domain V with boundary S , as depicted in Fig. 3, in which the base material occupied in sub-domain $\Omega (\Omega \subset V)$ with boundary Γ , imposing a macro strain E with periodic boundary conditions on the structure, a boundary value problem for sub-structure can be described as

$$\begin{cases} \operatorname{div} \sigma = \operatorname{div}(\mathbb{C}\nabla \mathbf{u}) = \mathbf{0} & \text{in } \Omega, \\ \mathbf{u}^+ - \mathbf{u}^- = \mathbf{E}(\mathbf{x}^+ - \mathbf{x}^-) & \text{on } \Gamma_u, \end{cases} \quad (1)$$

where σ is micro stress field, \mathbf{u} is the micro displacement field, \mathbf{x} is the location vector with respect to the center of the RVE, ∇ is the gradient operator, the symbols '+' and '-' denote the opposing sides of a RVE, and \mathbb{C} represents the elasticity tensor of the bulk material property. The macro stress Σ can be calculated by solving the above boundary value problem using

$$\Sigma = \frac{1}{V} \int_{\Omega^r} \sigma d\Omega. \quad (2)$$

The macro stress-strain relation for plane stress condition can be written as

$$\begin{bmatrix} \Sigma_{11} \\ \Sigma_{22} \\ \Sigma_{12} \end{bmatrix} = \frac{\bar{E}_Y}{1 - \bar{\nu}^2} \begin{bmatrix} 1 & \bar{\nu} & 0 \\ \bar{\nu} & 1 & 0 \\ 0 & 0 & \frac{1 - \bar{\nu}}{2} \end{bmatrix} \begin{bmatrix} E_{11} \\ E_{22} \\ 2E_{12} \end{bmatrix}. \quad (3)$$

where E^Y and $\bar{\nu}$ are the effective Young's modulus and Poisson's ratio, respectively.

Considering the case with a macro strain field of $E = [1, 0, 0]^T$, the effective Poisson's ratio can be evaluated after solving the boundary value problem shown in Eq. (1) using

$$\bar{\nu} = \frac{\Sigma_{22}}{\Sigma_{11}} = \frac{\int_{\Omega^r} \sigma_{22} d\Omega}{\int_{\Omega^r} \sigma_{11} d\Omega}. \quad (4)$$

and the effective Young's modulus can be evaluated using

$$\bar{E}^Y = \Sigma_{11} (1 - \bar{\nu}^2). \quad (5)$$

In this work, the boundary value problem shown in Eq. (1) is solved using isogeometric analysis that utilizes NURBS basis functions as the shape functions.

For a NURBS curve with an order of p , n control points and a knot vector $\Xi = [\xi_1, \xi_2, \dots, \xi_{n+p+1}]$, the weighted basis function corresponding to each control point is expressed as

$$N_{i,p}(\xi) = \frac{B_{i,p}(\xi)w_i}{\sum_{j=1}^n B_{j,p}(\xi)w_j}, \quad (6)$$

where the B-Spline basis $B_{i,p}(\xi)$ are defined as

$$B_{i,0}(\xi) = \begin{cases} 1, & \text{if } \xi_i \leq \xi < \xi_{i+1}, \\ 0, & \text{otherwise,} \end{cases} \quad (7)$$

$$B_{i,p}(\xi) = \frac{\xi - \xi_i}{\xi_{i+p} - \xi_i} B_{i,p-1}(\xi) + \frac{\xi_{i+p+1} - \xi}{\xi_{i+p+1} - \xi_{i+1}} B_{i+1,p-1}(\xi) \quad \text{if } \xi_i \leq \xi < \xi_{i+1}, \quad (8)$$

with the convention $0/0 = 0$. A 2D NURBS basis functions can be constructed as

$$N_{i,p}^{j,q}(\xi, \eta) = N_{i,p}(\xi)N_{j,q}(\eta), \quad (9)$$

where p and q denote the order in ξ and η direction, respectively. Accordingly, a generic variable x (e.g., coordinate, force, or displacement) can be interpolated from the corresponding control variables x_i with parametric coordinate (ξ, η) ,

$$x(\xi, \eta) = \sum_i N_i(\xi, \eta)x_i, \quad (10)$$

For example, in a deformed geometry patch, the displacement field \mathbf{u} can similarly be interpolated as

$$\mathbf{u} = \sum_i N_i \mathbf{u}_i, \quad (11)$$

where \mathbf{u}_i is the displacement value of the i th control point. Using this interpretation in FEM, the stiffness matrix ${}^i\mathbf{K}$, unknown displacement vector ${}^i\mathbf{U}$, and the corresponding load vector ${}^i\mathbf{F}$ for the i th NURBS patch can be obtained. By assembling them together with multiple

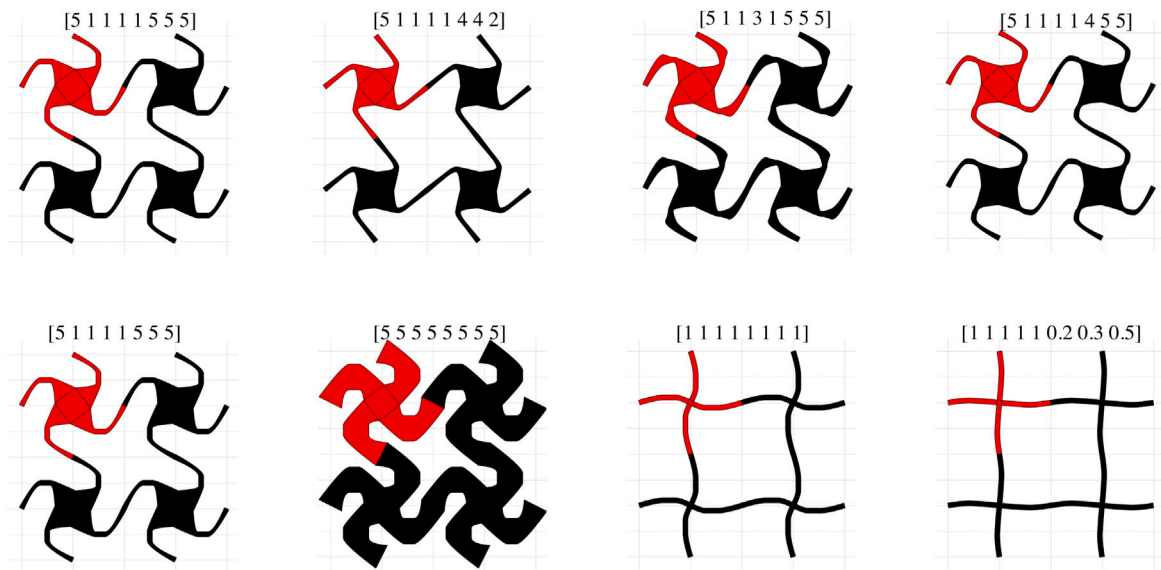


Fig. 2. Examples for tetra-chiral designs with different encoding parameters.

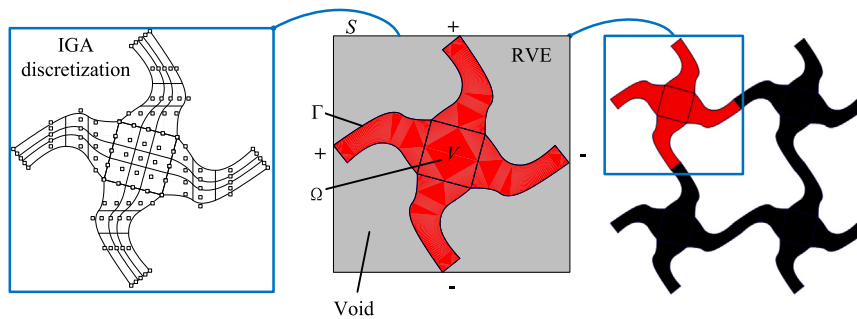


Fig. 3. The RVE of a tetra-chiral auxetic structure.

points constraints (MPCs), a system of equations can be obtained as

$$\begin{bmatrix} \mathbf{K} & \mathbf{A}^T \\ \mathbf{A} & 0 \end{bmatrix} \begin{bmatrix} \mathbf{U} \\ \lambda \end{bmatrix} = \begin{bmatrix} \mathbf{F} \\ \mathbf{b} \end{bmatrix}, \quad (12)$$

where λ are Lagrangian multipliers,

$$\mathbf{K} = \begin{bmatrix} {}^1\mathbf{K} & & & \\ & {}^2\mathbf{K} & & \\ & & \dots & \\ & & & {}^n\mathbf{K} \end{bmatrix}, \mathbf{U} = \begin{bmatrix} {}^1\mathbf{U} \\ {}^2\mathbf{U} \\ \dots \\ {}^n\mathbf{U} \end{bmatrix}, \text{ and } \mathbf{F} = \begin{bmatrix} {}^1\mathbf{F} \\ {}^2\mathbf{F} \\ \dots \\ {}^n\mathbf{F} \end{bmatrix}. \quad (13)$$

2.3. DNN-based surrogate model

The calculation cost of extracting the effective properties of tetra-chiral auxetics using IGA-based homogenization method can be cumbersome, and not favorable in designing variable auxeticity lattices with different local cell performances [79–82]. To promote computational efficiency, a deep neural network is introduced here. As a category of artificial neural network (ANN) [83] with multiple hiding layers, deep neural networks (DNN) are able to find a relatively accurate mathematical mapping from the input geometry parameters to the output effective properties. In this work, due to the complicated nonlinear relationship between the geometric parameters and effective mechanical properties for the tetra-chiral structures, it is important to use a proper deep learning structure to extract the complicated underlying relation. Compared with the shallow network, more hiding layers in DNN enables the composition of features from lower layers and modeling complex data with potentially fewer neuron units [84].

Consider a DNN with L layers, the input and output vectors in layer $l \in \{1, \dots, L\}$ are denoted \mathbf{z}^l and \mathbf{a}^l , respectively. The weights and biases from layer $l-1$ to l are denoted \mathbf{w}^l and \mathbf{b}^l , respectively. The feed-forward operation of DNN can be constructed as (for $l \in \{1, \dots, L-1\}$ and j denote any neuron unit)

$$\begin{aligned} z_j^{l+1} &= \mathbf{w}_j^{l+1} \mathbf{a}^l + b_j^{l+1}, \\ a_j^{l+1} &= \theta(z_j^{l+1}), \end{aligned} \quad (14)$$

where θ is activation function, representing hyperbolic tangent function *etanhe* in this work. As design variables have been limited into $\chi = [w_1, w_2, w_3, w_4, w_5, o_1, o_2, o_3]$, the input layer is set to have 8 neurons ($\mathbf{a}^1 = \chi$ is the input). The effective properties are effective Poisson's ratio and Young's modulus, leading to 2 output neurons (\mathbf{a}^L is the output). The DNN method in this work is a type of regression problem, which means that the output layer do not need to activated, hence, $\mathbf{a}^L = \mathbf{z}^L$. Eq. (14) can be rewritten in vector form as

$$\mathbf{a}^{l+1} = \theta(\mathbf{w}^{l+1} \mathbf{a}^l + \mathbf{b}^{l+1}). \quad (15)$$

The function of total training error is set in a quadratic norm as

$$C = \frac{1}{2n} \sum_x \|\mathbf{y} - \mathbf{a}^L\|^2, \quad (16)$$

where n denotes the total number of training examples, \mathbf{y} is the corresponding desired output.

The sensitivity analysis of the training error is performed using a back-propagation operation, which is simply to take the partial derivatives of training error C with respect to the weights w_i and the biases b_i .

For each training case, a error function δ_j^l of neuron j in layer l is defined as

$$\delta_j^l = \frac{\partial C}{\partial z_j^l}, \quad (17)$$

where δ^l represents the vector of errors associated with layer l . To compute δ^l for every layer, a recursive method is applied.

First, the output error δ_j^L in the output layer L reads,

$$\delta_j^L = \frac{\partial C}{\partial z_j^L} = \sum_k \frac{\partial C}{\partial a_k^L} \frac{\partial a_k^L}{\partial z_j^L}. \quad (18)$$

Note that the output activation a_k^L of the k th neuron is only determined by the weighted input z_k^L of the k th neuron. Hence, $\partial a_k^L / \partial z_j^L = 0$ when $k \neq j$. Recalling $a_j^L = z_j^L$, Eq. (18) can be simplified as

$$\delta_j^L = \frac{\partial C}{\partial a_j^L} \frac{\partial a_j^L}{\partial z_j^L} = \frac{\partial C}{\partial a_j^L}, \quad (19)$$

which can be written in a vector form as

$$\delta^L = \nabla_a C. \quad (20)$$

Then, the error δ_j^l can be represented in terms of the error of the next layer δ_j^{l+1}

$$\delta_j^l = \frac{\partial C}{\partial z_j^l} = \sum_k \frac{\partial C}{\partial z_k^{l+1}} \frac{\partial z_k^{l+1}}{\partial z_j^l} = \sum_k \frac{\partial z_k^{l+1}}{\partial z_j^l} \delta_k^{l+1}. \quad (21)$$

Note that

$$z_k^{l+1} = \sum_j w_{jk}^{l+1} a_j^l + b_k^{l+1} = \sum_j w_{jk}^{l+1} \theta(z_j^l) + b_k^{l+1}, \quad (22)$$

where w_{jk}^{l+1} is the weight from the j th neuron in the l th layer to the k th neuron in the $(l+1)$ th layer. Differentiating Eq. (22)

$$\frac{\partial z_k^{l+1}}{\partial z_j^l} = w_{jk}^{l+1} \theta'(z_j^l), \quad (23)$$

and substituting Eq. (23) to Eq. (21), the recursion relationship is obtained as

$$\delta_j^l = \sum_k w_{jk}^{l+1} \delta_k^{l+1} \theta'(z_j^l), \quad (24)$$

which can be written in a vector form as

$$\delta^l = \left((w^{l+1})^T \delta^{l+1} \right) \odot \theta'(z^l), \quad (25)$$

with \odot as the *Hadamard* product. Obviously, the gradient can be expressed as

$$\begin{aligned} \frac{\partial C}{\partial b_j^l} &= \delta_j^l, \\ \frac{\partial C}{\partial w_{kj}^l} &= a_k^{l-1} \delta_j^l. \end{aligned} \quad (26)$$

In the training process, the weights and the biases are updated using the following rules

$$\begin{aligned} w^l &\rightarrow w^l - \frac{\eta}{m} \sum_{\chi} \delta^l (a^{l-1})^T, \\ b^l &\rightarrow b^l - \frac{\eta}{m} \sum_{\chi} \delta^l, \end{aligned} \quad (27)$$

where η is learning rate and m is the number of training examples in a mini-batch.

The details of the DNN training are presented in Section 3. With a successful DNN training process, a DNN-based surrogate model (DSM) can be established to form a mapping between the geometry variables χ and the effective properties \mathbf{Y} , described as follows,

For each $l = 2, 3, \dots, L-1$ compute sequentially

$$\begin{aligned} z^l &= w^l a^{l-1} + b^l, \\ a^l &= \tanh(z^l), \end{aligned} \quad (28)$$

and in the output layer L ,

$$a^L = z^L = w^L a^{L-1} + b^L, \quad (29)$$

where $a^1 = \chi$ and $a^L = \mathbf{Y}$ (in which Y_1 denotes effective Poisson's ratio, and Y_2 denotes effective Young's modulus), all the weights and biases have been obtained via training previous.

2.4. Inverse design framework

Henceforth, a trained DSM replaces the complicated IGA-based computation homogenization and constructs an explicit function between geometric parameters and mechanical properties. Such a surrogate model not only facilitates the auxetic design to achieve NPR properties but also enables a fast, simple and straightforward design sensitivity analysis.

The inverse design optimization problem is to optimize a given tetra-chiral auxetic to achieve target Poisson's ratio with a restriction at a required stiffness, i.e.,

$$\min \Phi[\chi] := (\bar{\nu} - \check{\nu})^2 \quad (30)$$

subjected to

$$\begin{cases} \Psi_Y[\chi] := \bar{E}^Y - \check{E}^Y = 0 \\ \chi_i \in [\underline{\chi}_i, \bar{\chi}_i], \quad i = 1, 2, \dots, 8 \end{cases} \quad (31)$$

where $\Phi[\chi]$ is the cost function, $\check{\nu}$ is the target effective Poisson's ratio, \bar{E}^Y is the required effective Young's modulus, $\underline{\chi}_i$ and $\bar{\chi}_i$ are the lower and upper bounds of χ_i , respectively. To guarantee the optimal designs are meaningful and feasible, the lower and upper bounds are set as $\underline{\chi} = [0.1 \ 0.1 \ 0.1 \ 0.1 \ 0.1 \ 0 \ 0 \ 0]$ and $\bar{\chi} = [5 \ 5 \ 5 \ 5 \ 5 \ 5 \ 5 \ 5]$, respectively. A unit cell for the tetra-chiral structure has an area of 400, the initial design parameters is $[1 \ 1 \ 1 \ 1 \ 1 \ 0.1 \ 0.1 \ 0.1]$, which has an effective Poisson's ratio $\bar{\nu} = -0.0047$ and an effective Young's modulus $\bar{E}^Y = 4.88 \times 10^{-2} E_0^Y$, with E_0^Y denoting the Young's modulus of the base material.

The sensitivity analysis is represented as follows,

$$\dot{\Phi} = \frac{D\Phi}{D\chi_i} = 2(\bar{\nu} - \check{\nu})\dot{\bar{\nu}}, \quad (32)$$

where the dot over a variable denotes the material (design) derivative or full derivative. The gradient the effective Poisson's ratio $\dot{\bar{\nu}}$ (corresponding to a output neuron) with respect to the geometric parameters (the input neurons) can be obtained by

$$\dot{\bar{\nu}} = \frac{\partial Y_1}{\partial \chi_i}. \quad (33)$$

Similar to the approach used in the back-propagation in training the DNN, the gradient in Eq. (33) can also be calculated from layer L to layer 1. First, a recursive parameter $\epsilon^l = \partial Y_1 / \partial z^l$ is defined. In the output layer, the original value of ϵ^l is ϵ^L , which can be calculate by

$$\epsilon^L = \partial Y_1 / \partial z_1^L = 1. \quad (34)$$

Then, the values of ϵ^l for all layers can be calculated recursively using

$$\epsilon^l = \left((w^{l+1})^T \epsilon^{l+1} \right) \odot \theta'(z^l). \quad (35)$$

When $l = 2$,

$$z^2 = w^2 a^1 + b^2. \quad (36)$$

Note that $a^1 = \chi$, we have

$$\frac{\partial Y_1}{\partial \chi} = \frac{\partial Y_1}{\partial z^2} \frac{\partial z^2}{\partial a^1} = (w^2)^T \epsilon^2. \quad (37)$$

Henceforth, the derivative of effective Poisson ratio for i th input parameter is

$$\dot{\bar{\nu}} = \frac{\partial Y_1}{\partial \chi_i} = \sum_k w_{ki}^2 \epsilon_k^2. \quad (38)$$

Such explicit DSM allows an effective analytical derivation of the gradient that is difficult to achieve using IGA-based homogenization approach even with semi-analytical approach [53], and promotes the computing efficiency in optimization process significantly.

Based on the inverse design framework, the programmable designs with target properties and design limit exploration can be achieved. The flowchart of DSM-based inverse design framework is shown in Fig. 4.

3. The training process of deep neural network

The deep neural network (DNN) used in this work includes 7 layers, with an input layer consisting of 8 neurons (corresponding to the geometric parameter of tetra-chiral structure), 5 hidden layers, and an output layer consisting of 2 neurons (corresponding to the effective Poisson's ratio and Young's modulus). The parameters of DNN structure is 8-32-32-32-32-16-2, shown in Fig. 5a, in which each parameter denotes the number of neurons in the corresponding layer. It is noted that the DNN structure was chosen based on vast tests by balancing the training efficiency and accuracy. The training process and all numerical experiments were performed on a desktop computer with a GPU of NVIDIA GeForce GTX 1080, a CPU of Intel core i7-6700K, and a software environment of Matlab and TensorFlow.

Datasets are essential in a DNN training process and determine the upper limit of learning accuracy. In this work, three types of datasets (training set, validation set, and test set) were generated randomly using IGA-based homogenization. The training and validation sets were used in the training process of deep neural networks, while the test set is utilized to verify the accuracy of DSM. The sample numbers of the training, validation and test sets were 7000, 3000, and 500, respectively. It should be noted that all datasets have a similar distribution.

The offline computational cost for achieving the DSM on the above-mentioned computer is relatively cheap. The DNN training time takes approximately 15 min with the structure 8-32-32-32-32-16-2, while the training database costs around 90 min to generate 10000 random samples. The inverse design approach using DSM-based approach saves time in response evaluation and sensitivity analysis:

- The IGA-based homogenization normally takes a few seconds for one evaluation, while the DSM model outputs the results almost instantaneously.
- The IGA-homogenization-based inverse design approach uses finite difference to compute the sensitivity, which needs to run 8 simulations to obtain the gradient for the 7 design variables, while for the DSM-based approach, the analytical sensitivity analysis can be directly computed using the chain rule, with no simulation required.

The iterative history of the fitting error (defined in Eq. (16)) was plotted in Fig. 5b with an iteration number larger than 8000. The fitting errors for the training and validation sets dropped simultaneously during the iteration and converge at 0.000327 and 0.000589, respectively.

The test set including 500 random samples was applied to demonstrate the accuracy of DSM, in which the values obtained by homogenization and trained DSM were compared by histograms in Fig. 6a. It is clear that the data distributions of homogenization and DSM are similar, which proves the accuracy of DSM. The results obtained by trained DSM in the test set were validated using IGA-based homogenization method, as shown in Fig. 6b with the distribution of relative errors. It is noted that relative error is defined as

$$RE = \left| \frac{Y_i - a_i^L}{Y_i} \right|, \quad (39)$$

where Y_i is the effective mechanical property obtained by IGA-based homogenization approach, a_i^L is the corresponding value calculated by DSM, $i = 1$ denotes effective Poisson's ratio and $i = 2$ denotes effective

Young modulus. The average relative errors of the Poisson's ratio and Young's modulus are 0.038 and 0.008, respectively. As Fig. 6b showed, most samples locate within the area of tiny relative error, and the trained results of Young's modulus have better accuracy than that of the Poisson's ratio. The higher relative errors for the cases with Poisson's ratios close to 0 are mainly due to the fact that a smaller denominator of Y_i is prone to induce larger errors.

4. Results

4.1. Programmable designs with target properties

The DSM-based inverse design framework presented above can achieve programmable designs with target properties. To demonstrate its capability, three design study cases with the target effective Poisson's ratios of (i) $\check{\nu} = -0.5$, (ii) $\check{\nu} = -0.3$, and (iii) $\check{\nu} = 0$, respectively, subjected to a Young's modulus constraint of $\bar{E}^Y = 5.0 \times 10^{-2} E_0^Y$, are performed, and the optimized structures are shown in Fig. 7a and the optimized design variables are list in Appendix. The optimized solutions are further evaluated using the IGA-based homogenization method, which shows a good match towards the target properties. The target and constraints can be changed accordingly to achieve designs with programmable effective properties, which is essential for programming lattice structures with variable auxeticities [55].

In order to compare the optimization efficiency of DSM-based and homogenization-based approaches, the converging history of the first 10 steps with the same optimizer setting and the same target Poisson's ratio of $\check{\nu} = 0$ are depicted in Fig. 7b. The corresponding average computing time per step are 0.13 s and 5.29 s, respectively, demonstrating the high efficiency of the DSM-based approach. More importantly, the DSM-based approach also demonstrates a faster and smoother convergence. This significantly improves the efficiency of the inverse design process.

4.2. Design limit graphs

To explore the limits of programmable design over a range of stiffness constraints considering the lowest Poisson's ratio attainable (the lowest achievable Poisson's ratio at a given stiffness constraint), the target effective Poisson ratio $\check{\nu}$ was set as -1 . The design limit optimization was implemented sequentially over a range of \bar{E}^Y values for tetra-chiral auxetics. To demonstrate the efficiency and accuracy of proposed method, we compared the design limit curves obtained by conventional homogenization-based and DSM-based approaches, with the same stiffness restrictions from $\bar{E}^Y = 5 \times 10^{-5} E_0^Y$ to $1 \times 10^{-1} E_0^Y$. It is noted here that the homogenization-based approach utilizes finite difference method for design sensitivity analysis, while the DSM-based approach adopts a fully analytical approach. All the optimized parameter sets are re-evaluated using IGA-based homogenization to verify the feasibility. In Fig. 7c, the optimal results of the two categories are plotted along the design limit curves, and the corresponding optimized parameters for the solutions shown in Fig. 7c are listed in Appendix.

Note that the size of the ligaments gradually enlarges as stiffness constraint increases, indicating that large-size ligaments are beneficial to ensure the stiffness. Meanwhile the connection sizes (w_2, w_3) between core and ligaments are small to keep higher flexibility of rotations that promotes the auxeticity. From the design limit curves, it is clear that the DSM-based approach can achieve the same accuracy as the conventional homogenization approach, and possibly, can achieve even better results for some cases, possibly due to a more accurate sensitivity analysis.

In the interval $[10^{-6}, 10^{-3}]$ of the stiffness constraints, the limit curve using DSM-based approach is very close to the one using homogenization, with small differences of about ± 0.01 . In the interval $[10^{-3}, 10^{-1}]$,

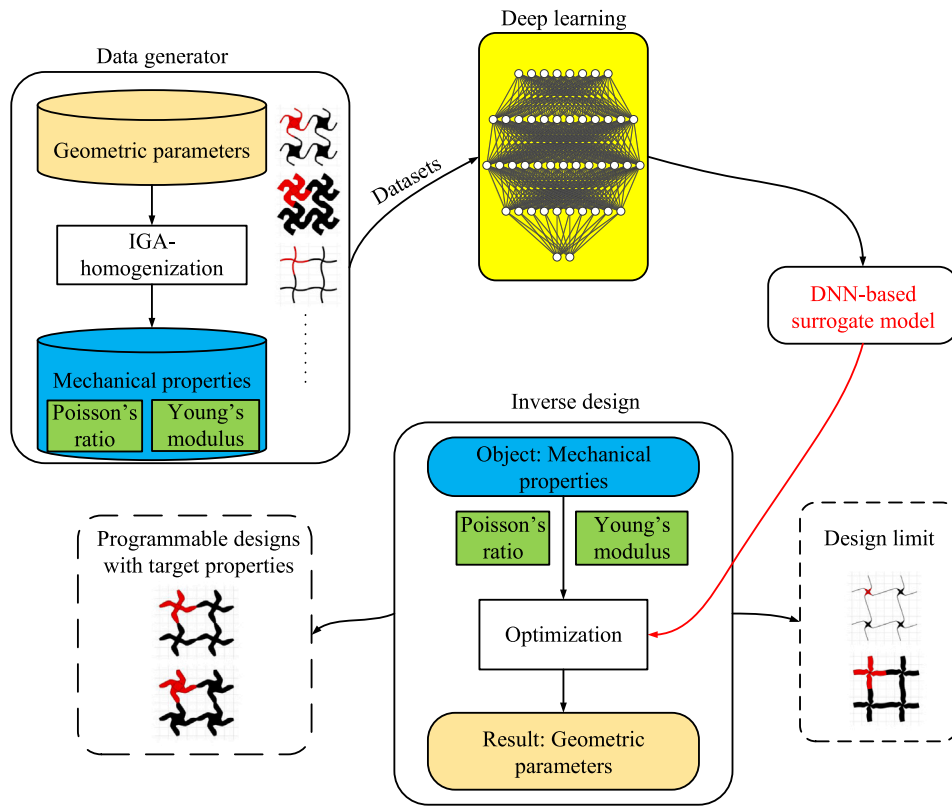


Fig. 4. The flowchart of the inverse design framework using DNN-based surrogate model.

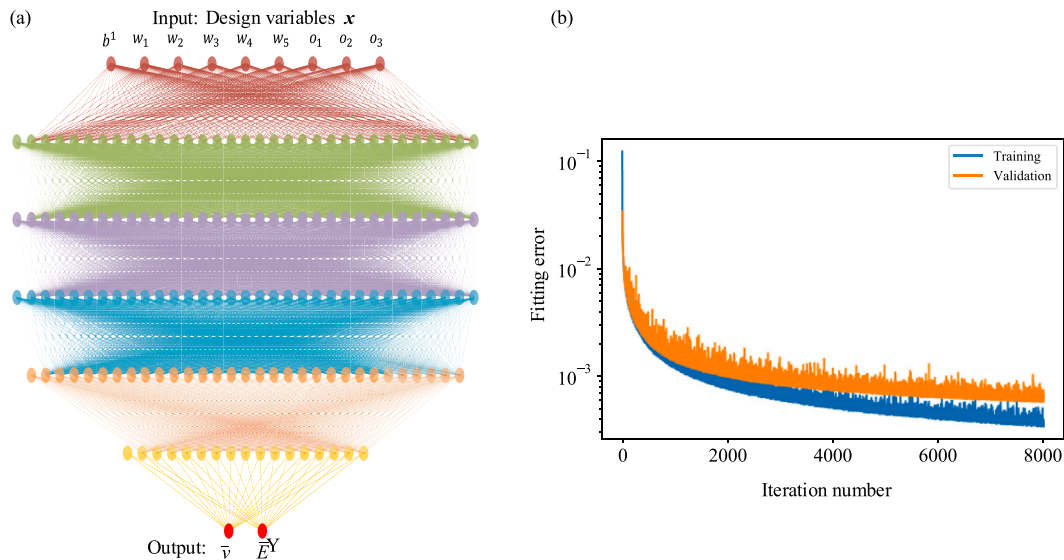


Fig. 5. DNN training: (a) the DNN structure and (b) the iteration history of fitting error.

the limit curve using DSM-based approach is better than that using homogenization-based approach, with a maximum improvement of -0.057 for the NPR. This is because the conventional homogenization-based approach may fall in local optimal results due to the limitations of finite difference sensitivity analysis, while the DNN approach with analytical sensitivity may provide a better search direction to achieve better results. However, in the interval $[10^{-6}, 10^{-3}]$, the points of DSM-based approach do not fulfill stiffness constraints perfectly, which may be caused by insufficient samples of training data in such region.

4.3. Verification

To verify the auxeticity of the tetra-chiral structures achieved using DSM-based inverse design approach, a configuration of specimen was chosen from the DSM-based design in Fig. 7c with a designed effective Poisson's ratio of -0.847 . The sample geometry generated using the DSM-based inverse design approach with a NURBS description was imported into ABAQUS (Version 2018) for analysis. The simulations in ABAQUS are performed with three different conditions: (i) compression

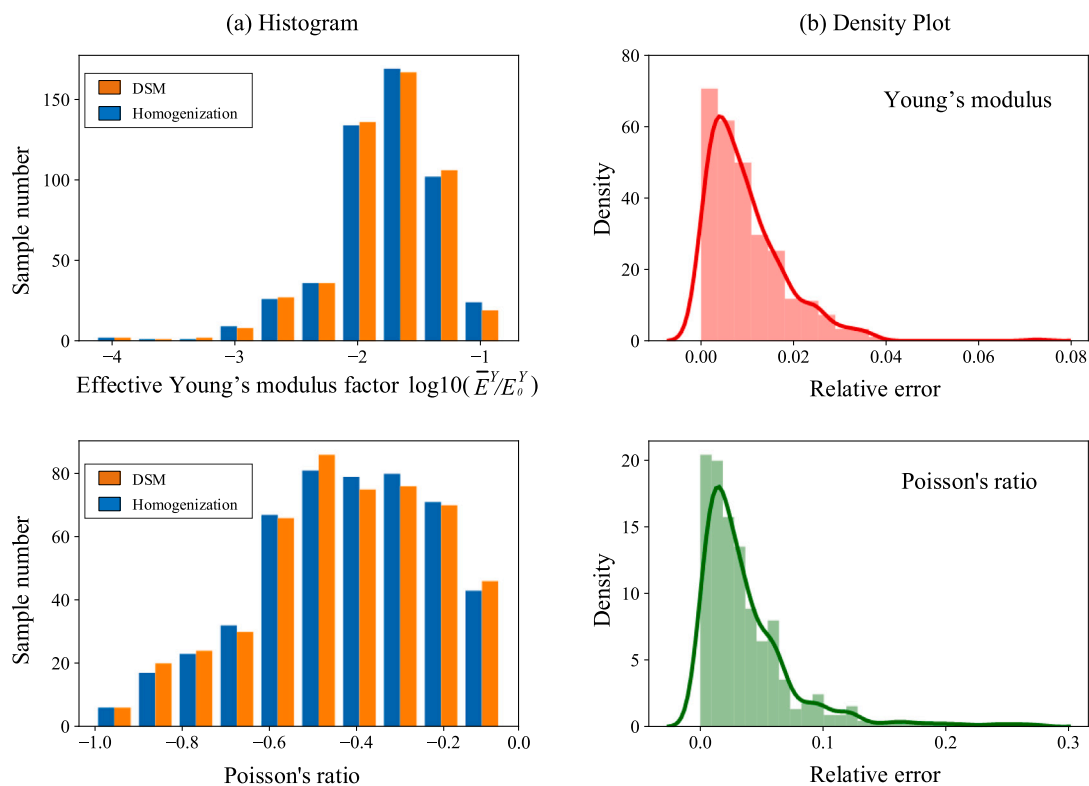


Fig. 6. Test set validation. (a) The data distributions comparison between homogenization and DSM values for test set. (b) The relative error distributions of DSM for test set (the area of rectangles represents the percentages of corresponding intervals).

up to -10% strain rate with a geometry nonlinear solver to evaluate the auxeticity under different compression strains, (ii) tension simulation with a linear solver to verify the effective Poisson's ratio under small deformation, and (iii) tension up to 10% strain rate with a geometry nonlinear solver to investigate the auxeticity variation under different tension strains. The simulation results are depicted in Fig. 8. It shows that for the chosen sample, the auxeticity in the simulated strain range increases under compression and decreases under tension, which is similar to the findings revealed in [85]. The linear simulation with an effective Poisson's ratio of -0.842 matches the DSM-based result very well, indicating the accuracy of the proposed DSM-based design approach.

5. Conclusion

In this work, we propose a deep-learning-based isogeometric inverse design framework for tetra-chiral auxetics, which is effective, systematic, and efficient. The DNN are trained utilizing the simulation database generated from an IGA-based homogenization of tetra-chiral auxetics with randomly distributed geometry parameters, which eventually forms an explicit DNN-based surrogate model (DSM) that provides a mapping from the geometric parameters to the effective properties. With this DSM, programmable auxetic designs with target properties can be achieved in an inverse design framework befitting from the high efficiency and the analytical sensitivity analysis of the DSM. Numerical studies are performed to verify the optimized solutions, demonstrating the availability, flexibility, and efficiency of the proposed design framework. It should be noted that the proposed method takes extra time for DNN training, however, the training process can be done offline and does not affect the efficiency of the inverse design approach. This work not only presents a novel method that harnesses simulated data and machine learning to design tetra-chiral auxetics but also can be potentially extended to multi-materials auxetics and other metamaterial designs, e.g. lattice materials [86,87],

acoustic materials [88,89] and other metamaterials [90–92]. Moreover, the concept in this work also indicates that a complicated physical mechanism can be expressed explicitly by machine learning methods, which bring significant benefits to tackle various inverse design problems in structures and materials, such as effective mechanical calculation, fast sensitive analysis and efficient optimization capability. Future work will be focused on fast-calculation methods for possible improved efficiency [93,94] and functionally graded structures design [55].

CRedit authorship contribution statement

Zhongyuan Liao: Methodology, Investigation, Data curation, Writing – original draft. **Yingjun Wang:** Conceptualization, Supervision, Writing – review & editing. **Liang Gao:** Supervision, Writing – review & editing. **Zhen-Pei Wang:** Software, Validation, Supervision, Writing – review & editing.

Declaration of competing interest

The authors declare that they have no known competing financial interests or personal relationships that could have appeared to influence the work reported in this paper.

Acknowledgment

This work has been supported by National Key R&D Program of China [No. 2020YFB1708300], National Natural Science Foundation of China [No. 52075184], Open-funding Project of State Key Laboratory of Digital Manufacturing Equipment and Technology (Huazhong University of Science and Technology) [No. DMETKF2021020]. These supports are gratefully acknowledged.

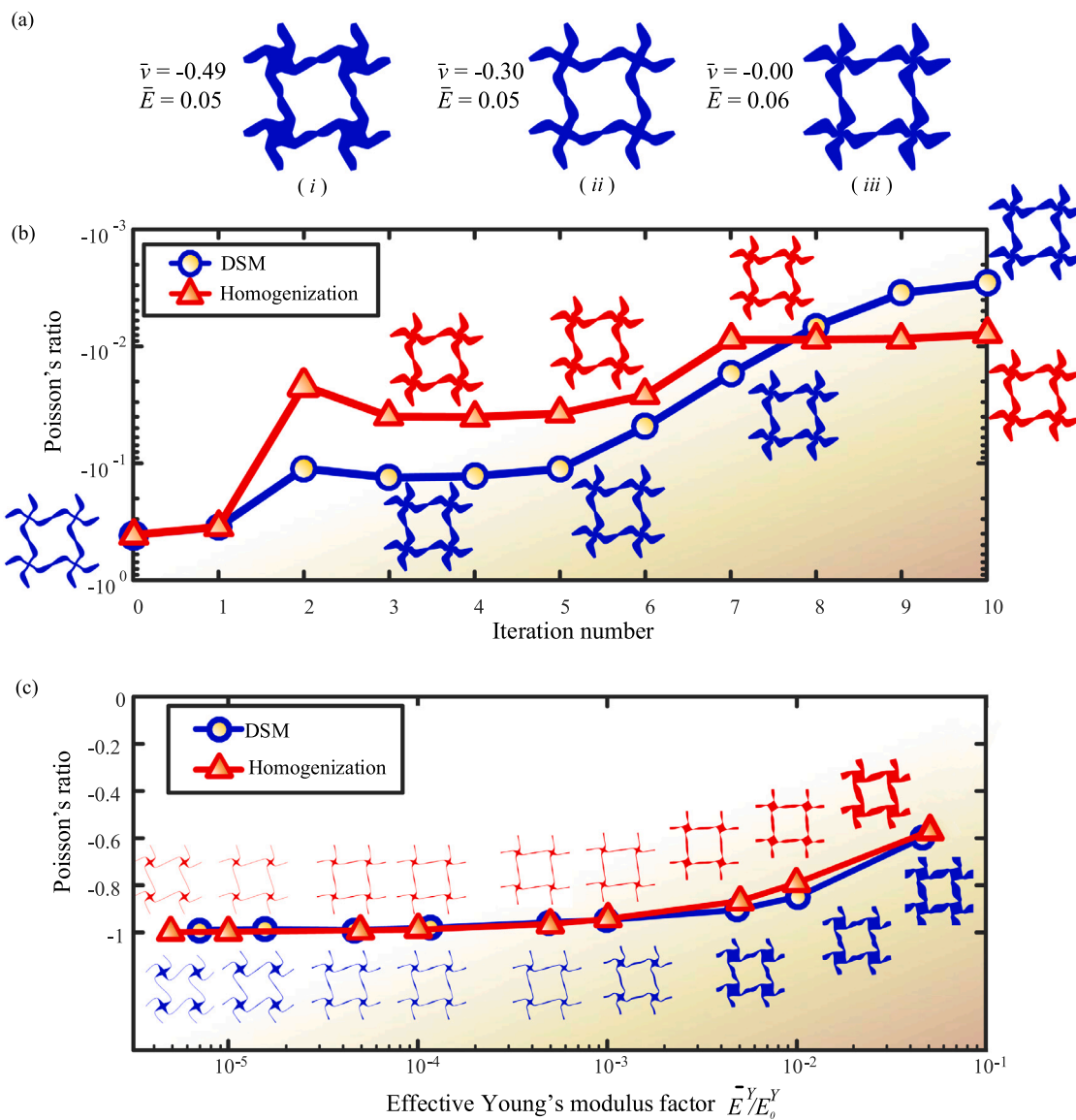


Fig. 7. Numerical study. (a) Programmable auxeticity designs with different target Poisson's ratios of (i) $\bar{\nu} = -0.5$, (ii) $\bar{\nu} = -0.3$, and (iii) $\bar{\nu} = 0$. (b) The converged history of DSM-based and homogenization-based approaches. (c) Design bounding graphs of the minimum achievable Poisson's ratio for the tetra-chiral auxetic structures.

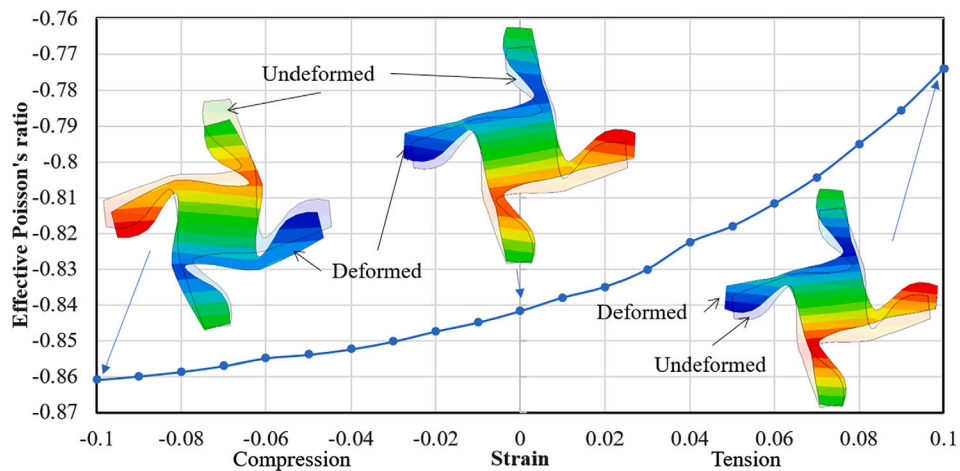


Fig. 8. Numerical verification in ABAQUS. For the chosen sample, the auxeticity in the simulated strain range increases under compression and decreases under tension. The linear simulation with an effective Poisson's ratio of -0.842 matches the DSM-based result very well.

Table A.1

The optimal design parameters of each optimized solution in Fig. 7a.

Cases	Design variables	Young's modulus	Poisson's ratios
i	[4.67 2.98 2.97 3.59 1.47 2.88 2.38 0.60]	0.05	-0.49
ii	[2.61 2.50 2.82 3.44 1.16 1.14 2.40 1.40]	0.05	-0.30
iii	[0.55 3.66 4.17 3.58 1.02 0.07 2.64 1.26]	0.06	-0.00

Table A.2

The design variables of optimized structures obtained by homogenization-based optimization methods in Fig. 7c (the red configurations from left to right).

Cases	Design variables	Young's modulus	Poisson's ratios
a	[1.53, 0.10, 0.10, 0.10, 0.10, 3.28, 2.85, 1.54]	5e-06	-0.998
b	[1.32, 0.10, 0.10, 0.10, 0.10, 2.21, 1.97, 1.05]	1e-05	-0.997
c	[1.50, 0.10, 0.10, 0.18, 0.56, 1.29, 1.19, 0.70]	5e-05	-0.991
d	[1.53, 0.21, 0.11, 0.15, 0.60, 1.34, 1.14, 0.55]	1e-04	-0.988
e	[1.60, 0.31, 0.31, 0.10, 0.68, 1.23, 1.09, 0.44]	5e-04	-0.965
f	[1.65, 0.33, 0.32, 0.28, 0.77, 1.15, 0.10, 0.38]	1e-03	-0.943
g	[2.83, 0.36, 0.22, 1.48, 1.21, 0.92, 0.55, 0.07]	5e-03	-0.867
h	[3.42, 0.19, 0.38, 2.17, 1.62, 0.74, 0.55, 0.18]	0.01	-0.790
i	[5.00, 1.67, 2.65, 4.50, 3.75, 2.63, 1.83, 0.65]	0.05	-0.570

Table A.3

The design variables of optimized structures obtained by DSM-based optimization method in Fig. 7c (the blue configurations from left to right).

Cases	Design variables	Young's modulus	Poisson's ratios
a	[2.34, 0.10, 0.14, 0.10, 0.11, 4.57, 4.94, 3.29]	7.08e-06	-0.990
b	[2.24, 0.10, 0.29, 0.10, 0.35, 3.62, 4.24, 2.21]	1.55e-05	-0.986
c	[1.65, 0.10, 0.18, 0.10, 0.78, 2.50, 2.24, 1.29]	4.63e-05	-0.990
d	[1.53, 0.10, 0.22, 0.10, 0.83, 2.30, 1.88, 1.18]	1.16e-04	-0.980
e	[1.48, 0.22, 0.48, 0.17, 0.88, 2.09, 1.63, 0.98]	4.89e-04	-0.957
f	[2.39, 0.15, 0.63, 0.96, 1.05, 2.37, 2.37, 0.40]	1.00e-03	-0.947
g	[5.00, 1.14, 0.90, 3.32, 2.02, 3.26, 2.74, 0.25]	4.80e-03	-0.905
h	[5.00, 1.04, 1.27, 3.91, 2.32, 3.06, 2.35, 0.25]	0.01	-0.847
i	[5.00, 0.89, 2.94, 5.00, 5.00, 2.21, 1.96, 0.00]	0.05	-0.598

Appendix. Optimized parameters of the solutions in Fig. 7.

See Tables A.1–A.3.

References

- Landau L, Lifshitz E, Kosevich A, Pitaevskii I. Theory of elasticity. London: Pergamon Press; 1986.
- Lim T-C. Auxetic materials and structures. Springer; 2015.
- Lim T-C. Auxetic microstructures. In: Mechanics of metamaterials with negative parameters. Springer; 2020, p. 9–51.
- Wojciechowski KW. Remarks on "Poisson ratio beyond the limits of the elasticity theory". J Phys Soc Japan 2003;72(7):1819–20.
- Goldstein R, Gorodtsov V, Lisovenko D. Auxetic mechanics of crystalline materials. Mech Solids 2010;45(4):529–45.
- Gorodtsov V, Lisovenko D. Auxetics among materials with cubic anisotropy. Mech Solids 2020;55(4):461–74.
- Homand-Etienne F, Houper R. Thermally induced microcracking in granites: characterization and analysis. Int J Rock Mech Min Sci Geomech Abstr 1989;26(2):125–34.
- Williams J, Lewis J. Properties and an anisotropic model of cancellous bone from the proximal tibial epiphysis. J Biomech Eng 1982;104(1):50–6.
- Veronda D, Westmann R. Mechanical characterization of skin—finite deformations. J Biomech 1970;3(1):111–24.
- Kumar D, Wang Z-P, Poh LH, Quek ST. Isogeometric shape optimization of smoothed petal auxetics with prescribed nonlinear deformation. Comput Methods Appl Mech Eng 2019;356:16–43.
- Kolpakov A. Determination of the average characteristics of elastic frameworks. J Appl Math Mech 1985;49(6):739–45.
- Almgren FR. An isotropic three-dimensional structure with Poisson's ratio = -1. J Elasticity 1985;15:427–30.
- Saxena KK, Das R, Calius EP. Three decades of auxetics research materials with negative Poisson's ratio: A review. Adv Energy Mater 2016;18(11):1847–70.
- Ren X, Das R, Tran P, Ngo TD, Xie YM. Auxetic metamaterials and structures: a review. Smart Mater Struct 2018;27(2):023001.
- Lakes R. Foam structures with a negative Poisson's ratio. Science 1987;235(4792):1038–40.
- Evans KE. Auxetic polymers: a new range of materials. Endeavour 1991;15(4):170–4.
- Wojciechowski KW. Constant thermodynamic tension Monte Carlo studies of elastic properties of a two-dimensional system of hard cyclic hexamers. Mol Phys 1987;61(5):1247–58.
- Wojciechowski KW. Two-dimensional isotropic system with a negative Poisson ratio. Phys Lett A 1989;137(1–2):60–4.
- Prall D, Lakes R, et al. Properties of a chiral honeycomb with a Poisson's ratio of -1. Int J Mech Sci 1997;39(3):305–14.
- Tretiakov KV, Wojciechowski KW. Auxetic, partially auxetic, and nonauxetic behaviour in 2D crystals of hard cyclic tetramers. Phys Status Solidi Rapid Res Lett 2020;14(7):2000198.
- Ha CS, Plesha ME, Lakes RS. Chiral three-dimensional lattices with tunable Poisson's ratio. Smart Mater Struct 2016;25(5):054005.
- Alderson A, Alderson KL, Attard D, Evans KE, Gatt R, Grima JN, et al. Elastic constants of 3-, 4- and 6-connected chiral and anti-chiral honeycombs subject to uniaxial in-plane loading. Compos Sci Technol 2010;70(7):1042–8.
- Bryukhanov I, Gorodtsov V, Lisovenko D. Modeling of the mechanical properties of chiral metallic nanotubes. Phys Mesomech 2020;23(6):477–86.
- Zhang H, Luo Y, Kang Z. Bi-material microstructural design of chiral auxetic metamaterials using topology optimization. Compos Struct 2018;195:232–48.
- Pozniak A, Wojciechowski KW. Poisson's ratio of rectangular anti-chiral structures with size dispersion of circular nodes. Phys Status Solidi B 2014;251(2):367–74.
- Jiang Y, Li Y. 3D printed chiral cellular solids with amplified auxetic effects due to elevated internal rotation. Adv Energy Mater 2017;19(2):1600609.
- Lakes RS. Negative-Poisson's-ratio materials: Auxetic solids. Annu Rev Mater Res 2017;47(1):63–81.
- Donoghue J, Alderson K, Evans K. The fracture toughness of composite laminates with a negative Poisson's ratio. Phys Status Solidi B 2009;246(9):2011–7.
- Duncan O, Shepherd T, Moroney C, Foster L, Venkatraman PD, Winwood K, et al. Review of auxetic materials for sports applications: Expanding options in comfort and protection. Appl Sci 2018;8(6):941.
- Wang Z, Hu H. Auxetic materials and their potential applications in textiles. Text Res J 2014;84(15):1600–11.
- Alderson A, Alderson K. Auxetic materials. Proc Inst Mech Eng G 2007;221(4):565–75.
- Ko J, Bhullar S, Cho Y, Lee PC, Jun MB-G. Design and fabrication of auxetic stretchable force sensor for hand rehabilitation. Smart Mater Struct 2015;24(7):075027.
- Theocaris P, Stavroulakis G, Panagiotopoulos P. Negative Poisson's ratios in composites with star-shaped inclusions: a numerical homogenization approach. Arch Appl Mech 1997;67(4):274–86.

- [34] Shokri Rad M, Ahmad Z, Alias A. Computational approach in formulating mechanical characteristics of 3D star honeycomb auxetic structure. *Adv Mater Sci Eng* 2015;2015.
- [35] Masters I, Evans K. Models for the elastic deformation of honeycombs. *Compos Struct* 1996;35(4):403–22.
- [36] Wang T, Wang L, Ma Z, Hulbert GM. Elastic analysis of auxetic cellular structure consisting of re-entrant hexagonal cells using a strain-based expansion homogenization method. *Mater Des* 2018;160:284–93.
- [37] Zhu Y, Wang Z-P, Poh LH. Auxetic hexachiral structures with wavy ligaments for large elasto-plastic deformation. *Smart Mater Struct* 2018;27(5):055001.
- [38] Mizzi L, Mahdi EM, Titov K, Gatt R, Attard D, Evans KE, et al. Mechanical metamaterials with star-shaped pores exhibiting negative and zero Poisson's ratio. *Mater Des* 2018;146:28–37.
- [39] Grima JN, Evans KE. Auxetic behavior from rotating squares. *J Mater Sci Lett* 2000;19(17):1563–5.
- [40] Dagdelen J, Montoya J, de Jong M, Persson K. Computational prediction of new auxetic materials. *Nature Commun* 2017;8(1):1–8.
- [41] Babaei S, Shim J, Weaver JC, Chen ER, Patel N, Bertoldi K. 3D soft metamaterials with negative Poisson's ratio. *Adv Mater* 2013;25(36):5044–9.
- [42] He Y, Zhou Y, Liu Z, Liew K. Pattern transformation of single-material and composite periodic cellular structures. *Mater Des* 2017;132:375–84.
- [43] Ren X, Shen J, Tran P, Ngo TD, Xie YM. Design and characterisation of a tuneable 3D buckling-induced auxetic metamaterial. *Mater Des* 2018;139:336–42.
- [44] Prawoto Y. Seeing auxetic materials from the mechanics point of view: a structural review on the negative Poisson's ratio. *Comput Mater Sci* 2012;58:140–53.
- [45] Sigmund O. Materials with prescribed constitutive parameters: an inverse homogenization problem. *Int J Solids Struct* 1994;31(17):2313–29.
- [46] Xia L, Breitkopf P. Design of materials using topology optimization and energy-based homogenization approach in Matlab. *Struct Multidiscip Optim* 2015;52(6):1229–41.
- [47] Wang F. Systematic design of 3D auxetic lattice materials with programmable Poisson's ratio for finite strains. *J Mech Phys Solids* 2018;114:303–18.
- [48] Schwerdtfeger J, Wein F, Leugering G, Singer RF, Körner C, Stingl M, et al. Design of auxetic structures via mathematical optimization. *Adv Mater* 2011;23(22–23):2650–4.
- [49] Czarnecki S, Lukasiak T. Recovery of the auxetic microstructures appearing in the least compliant continuum two-dimensional bodies. *Phys Status Solidi B* 2020;257(10):1900676.
- [50] Clausen A, Wang F, Jensen JS, Sigmund O, Lewis JA. Topology optimized architectures with programmable Poisson's ratio over large deformations. *Adv Mater* 2015;27(37):5523–7.
- [51] Wang C, Xia S, Wang X, Qian X. Isogeometric shape optimization on triangulations. *Comput Methods Appl Mech Engrg* 2018;331:585–622.
- [52] Wang Z-P, Poh LH, Dirrenberger J, Zhu Y, Forest S. Isogeometric shape optimization of smoothed petal auxetic structures via computational periodic homogenization. *Comput Methods Appl Mech Engrg* 2017;323:250–71.
- [53] Wang Z-P, Poh LH. Optimal form and size characterization of planar isotropic petal-shaped auxetics with tunable effective properties using IGA. *Compos Struct* 2018;201:486–502.
- [54] Wang Y, Wang Z-P, Xia Z, Poh LH. Structural design optimization using isogeometric analysis: a comprehensive review. *CMES Comput Model Eng Sci* 2018;455–507.
- [55] Wang Z-P, Poh LH, Zhu Y, Dirrenberger J, Forest S. Systematic design of tetra-petals auxetic structures with stiffness constraint. *Mater Des* 2019;170:107669.
- [56] Choi M-J, Cho S. Isogeometric configuration design optimization of shape memory polymer curved beam structures for extremal negative Poisson's ratio. *Struct Multidiscip Optim* 2018;58(5):1861–83.
- [57] Wu J, Sigmund O, Groen JP. Topology optimization of multi-scale structures: a review. *Struct Multidiscip Optim* 2021;1–26.
- [58] Zuo ZH, Huang X, Rong JH, Xie YM. Multi-scale design of composite materials and structures for maximum natural frequencies. *Mater Des* 2013;51:1023–34.
- [59] Li Y, Feng Z, Hao L, Huang L, Xin C, Wang Y, et al. A review on functionally graded materials and structures via additive manufacturing: From multi-scale design to versatile functional properties. *Adv Mater Technol* 2020;5(6):1900981.
- [60] Le BA, Yvonnet J, He QC. Computational homogenization of nonlinear elastic materials using neural networks. *Internat J Numer Methods Engrg* 2015;104(12):1061–84.
- [61] Gu GX, Chen C-T, Buehler MJ. De novo composite design based on machine learning algorithm. *Extreme Mech Lett* 2018;18:19–28.
- [62] Liu Z, Wu CT, Koishi M. A deep material network for multiscale topology learning and accelerated nonlinear modeling of heterogeneous materials. *Comput Methods Appl Mech Engrg* 2019;345:1138–68.
- [63] Liu Z, Wu CT. Exploring the 3D architectures of deep material network in data-driven multiscale mechanics. *J Mech Phys Solids* 2019;127:20–46.
- [64] Li H, Kafka OL, Gao J, Yu C, Nie Y, Zhang L, et al. Clustering discretization methods for generation of material performance databases in machine learning and design optimization. *Comput Mech* 2019;64(2):281–305.
- [65] Mao Y, He Q, Zhao X. Designing complex architected materials with generative adversarial networks. *Sci Adv* 2020;6(17):eaaz4169.
- [66] Wilt JK, Yang C, Gu GX. Accelerating auxetic metamaterial design with deep learning. *Adv Energy Mater* 2020;22(5):1901266.
- [67] Kollmann HT, Abueidda DW, Koric S, Guleryuz E, Sobh NA. Deep learning for topology optimization of 2D metamaterials. *Mater Des* 2020;196:109098.
- [68] Wang H, Xiao S-H, Zhang C. Novel planar auxetic metamaterial perforated with orthogonally aligned oval-shaped holes and machine learning solutions. *Adv Energy Mater* 2021;23(7):2100102.
- [69] Banga S, Gehani H, Bhilare S, Patel S, Kara L. 3D topology optimization using convolutional neural networks. 2018, ArXiv:1808.07440.
- [70] Sosnovik I, Oseledets I. Neural networks for topology optimization. *Russian J Numer Anal Math Modelling* 2019;34(4):215–23.
- [71] Yu Y, Hur T, Jung J, Jang IG. Deep learning for determining a near-optimal topological design without any iteration. *Struct Multidiscip Optim* 2019;59(3):787–99.
- [72] Cang R, Yao H, Ren Y. One-shot generation of near-optimal topology through theory-driven machine learning. *Comput Aided Des* 2019;109:12–21.
- [73] Lei X, Liu C, Du Z, Zhang W, Guo X. Machine learning-driven real-time topology optimization under moving morphable component-based framework. *J Appl Mech* 2018;86(1).
- [74] Ulu E, Zhang R, Kara LB. A data-driven investigation and estimation of optimal topologies under variable loading configurations. *Comput Methods Biomech Biomed Eng Imag Visual* 2016;4(2):61–72.
- [75] Oh S, Jung Y, Kim S, Lee I, Kang N. Deep generative design: Integration of topology optimization and generative models. *J Mech Des* 2019;141(11):111405.
- [76] Wang Y, Liao Z, Shi S, Wang Z-P, Poh LH. Data-driven structural design optimization for petal-shaped auxetics using isogeometric analysis. *CMES Comput Model Eng Sci* 2020;122(2):433–58.
- [77] Cappelli L, Montemurro M, Dau F, Guillaume L. Characterisation of composite elastic properties by means of a multi-scale two-level inverse approach. *Compos Struct* 2018;204:767–77.
- [78] Wang G, Dong L, Atluri SN. Direct and inverse multi-scale analyses of arbitrarily functionally graded layered hollow cylinders (discs), with different shaped reinforcements, under harmonic loads. *Compos Struct* 2018;188:425–37.
- [79] Wu Z, Xia L, Wang S, Shi T. Topology optimization of hierarchical lattice structures with substructuring. *Comput Methods Appl Mech Engrg* 2019;345:602–17.
- [80] Paulino GH, Silva ECN, Le CH. Optimal design of periodic functionally graded composites with prescribed properties. *Struct Multidiscip Optim* 2009;38(5):469–89.
- [81] Radman A, Huang X, Xie YM. Topology optimization of functionally graded cellular materials. *J Mater Sci* 2013;48(4):1503–10.
- [82] Li H, Luo Z, Gao L, Walker P. Topology optimization for functionally graded cellular composites with metamaterials by level sets. *Comput Methods Appl Mech Engrg* 2018;328:340–64.
- [83] Schmidhuber J. Deep learning in neural networks: An overview. *Neural Netw* 2015;61:85–117.
- [84] Bengio Y. Learning deep architectures for AI. In: *Foundations and trends® in machine learning*. 2, (1):2009, p. 1–127.
- [85] Wang F, Sigmund O, Jensen JS. Design of materials with prescribed nonlinear properties. *J Mech Phys Solids* 2014;69:156–74.
- [86] Wang Y, Arabnejad S, Tanzer M, Pasini D. Hip implant design with three-dimensional porous architecture of optimized graded density. *J Mech Des* 2018;140(11):111406.
- [87] Da D, Yvonnet J, Xia L, Le MV, Li G. Topology optimization of periodic lattice structures taking into account strain gradient. *Comput Struct* 2018;210:28–40.
- [88] Lee J-H, Koh CY, Singer JP, Jeon S-J, Maldovan M, Stein O, et al. 25th anniversary article: Ordered polymer structures for the engineering of photons and phonons. *Adv Mater* 2014;26(4):532–69.
- [89] Lee SH, Park CM, Seo YM, Wang ZG, Kim CK. Acoustic metamaterial with negative modulus. *J Phys: Condens Matter* 2009;21(17):175704.
- [90] Zheng Y, Wang Y, Lu X, Liao Z, Qu J. Evolutionary topology optimization for mechanical metamaterials with auxetic property. *Int J Mech Sci* 2020;105638.
- [91] Yu X, Zhou J, Liang H, Jiang Z, Wu L. Mechanical metamaterials associated with stiffness, rigidity and compressibility: A brief review. *Prog Mater Sci* 2018;94:114–73.
- [92] Da D, Qian X. Fracture resistance design through biomimicry and topology optimization. *Extreme Mech Lett* 2020;40:100890.
- [93] Liao Z, Zhang Y, Wang Y, Li W. A triple acceleration method for topology optimization. *Struct Multidiscip Optim* 2019;60(2):727–44.
- [94] Wang Y, Liao Z, Ye M, Zhang Y, Li W, Xia Z. An efficient isogeometric topology optimization using multilevel mesh, MGCG and local-update strategy. *Adv Eng Softw* 2020;139:102733.